



UNIVERSITÀ  
DEGLI STUDI  
FIRENZE

# FLORE

## Repository istituzionale dell'Università degli Studi di Firenze

### **Evaporation and fission decay of (132)Ce compound nuclei at $E(x)=122$ MeV: some limitations of the statistical model**

Questa è la Versione finale referata (Post print/Accepted manuscript) della seguente pubblicazione:

*Original Citation:*

Evaporation and fission decay of (132)Ce compound nuclei at  $E(x)=122$  MeV: some limitations of the statistical model / Di Nitto, A.; Vardaci, E.; Brondi, A.; La Rana, G.; Moro, R.; Nadtochy, P. N.; Trotta, M.; Ordine, A.; Boiano, A.; Cinausero, M.; Fioretto, E.; Prete, G.; Rizzi, V.; Shetty, D. V.; Barbui, M.; Fabris, D.; Lunardon, M.; Montagnoli, G.; Moretto, S.; Viesti, G.; Gelli, N.; Lucarelli, Franco; Knyazheva, G. N.; Kozulin, E. M.. - In: THE EUROPEAN PHYSICAL JOURNAL. A, HADRONS AND NUCLEI. - ISSN 1434-6001. - STAMPA. -

*Availability:*

This version is available at: 2158/495660 since:

*Published version:*

DOI: 10.1140/epja/i2011-11083-6

*Terms of use:*

Open Access

La pubblicazione è resa disponibile sotto le norme e i termini della licenza di deposito, secondo quanto stabilito dalla Policy per l'accesso aperto dell'Università degli Studi di Firenze (<https://www.sba.unifi.it/upload/policy-oa-2016-1.pdf>)

*Publisher copyright claim:*

(Article begins on next page)

Eur. Phys. J. A (2011) 47: 83

DOI: 10.1140/epja/i2011-11083-6

## Evaporation and fission decay of $^{132}\text{Ce}$ compound nuclei at $E_x=122$ MeV: some limitations of the statistical model

A. Di Nitto, E. Vardaci, A. Brondi, G. La Rana, R. Moro, P.N. Nadtochy, M. Trotta, A. Ordine, A. Boiano, M. Cinausero, E. Fioretto, G. Prete, V. Rizzi, D.V. Shetty, M. Barbui, D. Fabris, M. Lunardon, G. Montagnoli, S. Moretto, G. Viesti, N. Gelli, F. Lucarelli, G.N. Knyazheva and E.M. Kozulin



Springer

# Evaporation and fission decay of $^{132}\text{Ce}$ compound nuclei at $E_x=122$ MeV: some limitations of the statistical model

A. Di Nitto<sup>1</sup>, E. Vardaci<sup>1</sup>, A. Brondi<sup>1</sup>, G. La Rana<sup>1</sup>, R. Moro<sup>1,a</sup>, P.N. Nadtochy<sup>2,b</sup>, M. Trotta<sup>2</sup>, A. Ordine<sup>2</sup>, A. Boiano<sup>2</sup>, M. Cinausero<sup>3</sup>, E. Fioretto<sup>3</sup>, G. Prete<sup>3</sup>, V. Rizzi<sup>3</sup>, D.V. Shetty<sup>3,c</sup>, M. Barbui<sup>4,d</sup>, D. Fabris<sup>4</sup>, M. Lunardon<sup>4</sup>, G. Montagnoli<sup>4</sup>, S. Moretto<sup>4</sup>, G. Viesti<sup>4</sup>, N. Gelli<sup>5</sup>, F. Lucarelli<sup>5</sup>, G.N. Knyazheva<sup>6</sup> and E.M. Kozulin<sup>6</sup>

<sup>1</sup> Istituto Nazionale di Fisica Nucleare and Dipartimento di Scienze Fisiche, Università di Napoli “Federico II”, Via Cinthia, 80126 Napoli, Italy

<sup>2</sup> Istituto Nazionale di Fisica Nucleare, Via Cinthia, 80126 Napoli, Italy

<sup>3</sup> Laboratori Nazionali di Legnaro dell’Istituto Nazionale di Fisica Nucleare, Legnaro (Padova), Italy

<sup>4</sup> Istituto Nazionale di Fisica Nucleare and Dipartimento di Fisica, Padova, Italy

<sup>5</sup> Istituto Nazionale di Fisica Nucleare and Dipartimento di Fisica, Firenze, Italy

<sup>6</sup> Flerov Laboratory of Nuclear Reactions, Joint Institute for Nuclear Research, RU-141980 Dubna, Moscow Region, Russia

Received: 17 May 2011 / Revised: 15 June 2011

Published online: 30 June 2011 – © Società Italiana di Fisica / Springer-Verlag 2011

Communicated by C. Signorini

**Abstract.** Light charged particle (LCP) emission in the evaporation residue (ER) and fusion fission (FF) channels have been studied for the 200 MeV  $^{32}\text{S} + ^{100}\text{Mo}$  reaction, leading to  $^{132}\text{Ce}$  composite nuclei at  $E_x=122$  MeV. The main goal was to study the decay of  $^{132}\text{Ce}$  on the basis of an extended set of observables, to get insights on the fission dynamics. The proton and alpha particle energy spectra, their multiplicities, ER-LCP angular correlations, ER and FF angular distributions, and ER and FF cross-sections were measured. The measured observables were compared with the Statistical Model (SM). Using standard parameters, the model was able to reproduce only the pre-scission multiplicities and the FF and ER cross-sections. The calculation was observed to strongly overestimate the proton and alpha particle multiplicities in the ER channel. Disagreements were also observed for the ER-LCP correlations, the LCP energy spectra and the ER angular distribution. By varying the SM input parameters over a wide range of values, it is shown that it is not possible to reproduce all the observables simultaneously with a unique set of parameters. The inadequacy of the model in reproducing the ER particle multiplicities is also observed analysing data from the literature for other systems in the  $A \approx 150$  and  $E_x \approx 100\text{--}200$  MeV region. These results indicate serious limitations about the use of the SM in extracting information on fission dynamics.

## 1 Introduction

The Statistical Model (SM) is widely used to support the picture of a heavy-ion-induced fission process governed by nuclear viscosity [1–12]. The excess of measured pre-scission light particles and GDR  $\gamma$ -rays multiplicities with respect to the expected values determined by the SM is usually ascribed to the increment of the lifetime of the hot fissioning nucleus because of the viscosity of the nuclear matter, a physical ingredient not included in the SM. Sev-

eral extensions of the SM have been proposed to take into account the hypothetical larger time scale of the fission process. In the simplest fashion, the SM is modified to include one more parameter, the fission delay  $\tau_d$ . During the evaporative decay chain, that includes competition between particles and fission decay modes, the fission width is kept to zero for a time  $\tau_d$  above which the fission width is set to the full value given by Bohr-Wheeler model. Light-particles evaporation and GDR  $\gamma$ -rays are consequently favored at the beginning of the decay chain because of the artificial hindrance of the fission probability, and larger pre-scission multiplicities are achieved.

This transient mechanism that simulates the presence of nuclear viscosity can indeed trigger a variety of other effects of dynamical origin, among which the possibility that a compound nucleus committed to fission (namely, already at the saddle point configuration) can still become an evaporation residue if enough particles are evaporated

<sup>a</sup> e-mail: moro@na.infn.it

<sup>b</sup> Permanent address: Omsk State University, Department of Theoretical Physics, Mira prospekt 55-A, Omsk, 644077, Russia.

<sup>c</sup> Present address: Department of Physics, Western Michigan University, Kalamazoo, MI 49008, USA.

<sup>d</sup> Present address: Cyclotron Institute, Texas A&M University, College Station TX 77843 USA.

and the fissility and angular momentum reduced. The correlation between the enhanced yield of pre-scission particles and the survival of evaporation residues might be an important channel, in the mass region  $A \approx 150\text{--}160$ , for the feeding of ER having large deformations [5].

Estimates of  $\tau_d$  are extracted by adjusting the pre-scission multiplicities predicted by the SM, which includes this new parameter, to those obtained experimentally. The reported values of the fission delay time, however, range from zero [2] to  $500 \times 10^{-21}$  s [4] depending on the mass region, the excitation energy and the experimental probes. Often it is reported that it is necessary to intervene on other crucial ingredients of the SM, not the fission delay alone, in the attempt to reproduce the pre-scission multiplicities of the probes of interest. These ingredients involve the level density, the transmission coefficients and the fission barrier models. Furthermore, estimates of  $\tau_d$ , or the fission time scale of the specific model, are often quite blurred by the fact that different sets of input parameters provide equally good fit to the data within the same model [3, 9, 10].

It was pointed out in ref. [7] that, besides the evident limit of a static description of a dynamical process like the fission within the SM, more reliable estimates of the fission delay might be obtained if more constraints to the relevant input parameters are provided, and this can be accomplished by including additional observables into the data set to be compared with the SM calculations. It was further proposed that systems of intermediate fissility ( $A \approx 100\text{--}180$ ) could provide an effective environment for such a test. Compared to the heavier systems, those of intermediate fissility have larger pre-scission charged-particle multiplicities as well as comparable fission and ER cross-sections. Since the possibility of a hindered fission results in an increment of the ER cross-section, the light-particle multiplicities in the ER channel, along with the ER integral cross-section, are proposed as potentially informative observables on the fission process. However, this kind of approach is founded on the reliability of the SM to reproduce the observables in the ER channel, and this has not yet been fully explored.

In this framework, our collaboration has undertaken a research program aimed at studying the fission dynamics in systems of intermediate fissility. In a previous work [12], the decay of the compound nucleus  $^{132}\text{Ce}$ , produced by the 240 MeV  $^{32}\text{S} + ^{100}\text{Mo}$  reaction, at  $E_x = 152$  MeV was studied. It was shown that the measured pre-scission alpha particle multiplicity could be reproduced by the SM calculations without the inclusion of a fission delay time, regardless of the fact that a fission delay was expected on the basis of a systematic study [13]. It was however argued [12] that fast fission could have been responsible for such a result. To probe this hypothesis an experiment at a lower energy, where fast fission is expected to be negligible, was therefore planned.

Here we report on the measurement of the evaporation and fission decay of the compound nucleus  $^{132}\text{Ce}$  at  $E_x = 122$  MeV, produced by the 200 MeV  $^{32}\text{S} + ^{100}\text{Mo}$  reaction and on a SM model analysis performed on a

large set of observables. A short presentation of the data analysis and conclusions has already been published as a letter [14]. Here we discuss in detail the experimental methods for the extraction of the various observables that we measured in the ER and FF channels, namely proton and alpha particles energy spectra in coincidence with FF and ER, multiplicities, angular distributions, and ER and FF channels cross-sections. The measured quantities were compared with the SM calculations carried out by changing many physical ingredients of the model. The present paper is organized as follows: in sect. 2 we describe the experimental setups, the measurements of the ER and FF absolute cross-sections and the models used to extract experimental data; in sect. 3 we describe in detail the data analysis procedures and present the most important data; in sect. 4 we propose an extensive SM analysis of a large set of observables; in sect. 5 we draw the conclusions.

## 2 Experimental setup

### 2.1 Measurement of light charged particles in coincidence with ER or FF fragments

The experiment was performed at the XTU Tandem-ALPI Superconducting LINAC accelerator complex of the Laboratori Nazionali di Legnaro. A 200 MeV pulsed beam of  $^{32}\text{S}$  of intensity of about 1–3 enA was used to bombard a self-supporting  $^{100}\text{Mo}$  target 400  $\mu\text{g}/\text{cm}^2$  thick. A beam burst with a period of 800 ns and duration of about 3 ns was used. We used the BALL section of the  $8\pi$  LP apparatus [15], to detect light charged particles (LCPs) in single mode and coincidence with ER and FF. The BALL, shown schematically in fig. 1, has a diameter of 30 cm and consists of 7 rings of detectors placed coaxially around the beam direction. Each ring, labeled from A to G going from backward to forward angles, contains 18 two-stage  $\Delta E$ - $E$  telescopes pointing towards the center of the target, and covers an angular opening of about  $17^\circ$ . Each telescope is made of a 300  $\mu\text{m}$ -Si detector, mounted in the so-called *flipped* configuration (particle entering from the rear side), backed by a 15mm CsI(Tl) crystal. The full BALL has a total of 126 telescopes and covers the polar angle from  $34^\circ$  to  $165^\circ$ . Considering this geometry, the detectors in a ring have the same average polar angle with respect to the beam direction axis, and all together cover the azimuthal angle from  $0^\circ$  to  $360^\circ$ . As a whole the BALL covers a solid angle of about 80% of  $4\pi$ .

Energy calibration of  $\Delta E$  detectors is carried out by using an Am-Cm  $\alpha$ -source and a pulser. The energy calibration of the CsI(Tl) detectors is accomplished with a specifically developed procedure that relies on the knowledge of the thickness of each Si detector and on the stopping power tables [16].

Particle identification is carried out by using the  $\Delta E$ - $E$  technique for the particles that have energy enough to pass through the  $\Delta E$  stage. The Pulse Shape Discrimination (PSD) technique is instead used for the particles that stop in the Si detector. This is the reason for the choice of the *flipped* configuration of the Si detectors of the BALL.

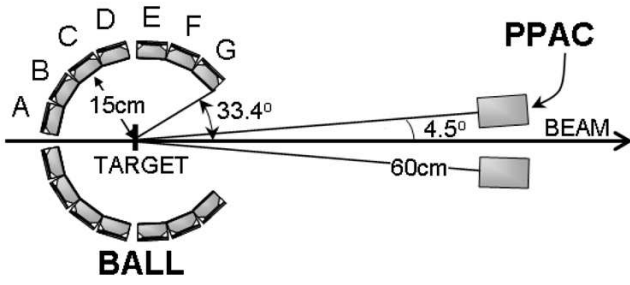


Fig. 1: Schematic layout of the experimental apparatus. The letters from A to G label the 7 rings of detectors.

For the reaction under study we were able to identify the charged particles with energy thresholds of 0.5 MeV for protons and 1 MeV for alpha particles.

In the present experiment, evaporation residues were detected by four Parallel Plate Avalanche Counter (PPAC) modules, placed in four symmetric positions with respect to the beam direction axis, two in the horizontal plane (named PPAC-left and PPAC-right) and the other two in the vertical plane (named PPAC-up and PPAC-down). Each PPAC module consists, indeed, of two coaxial PPACs (front and rear) operating in the same gas volume at the pressure of about 40 Torr and mounted at the distance of 15 cm from each other. This gas pressure was sufficient to stop the ER between the two PPACs, and let the other ions, like FF and elastic scattered beam particles, reach the rear PPAC. ER are therefore selected by a vetoed TOF technique: the time between the beam RF signal and the signal from the front PPAC is recorded if the signal from the rear PPAC is missing. This method allows to reject, with high efficiency, signals due to ions reaching the rear PPAC which are much faster and much lighter than the evaporation residues. Each PPAC module was positioned at  $4.5^\circ$  with respect to the beam direction and subtended a solid angle of 0.8 msr.

The heavy fragments produced in the reaction were detected in the telescopes of the most forward rings of the BALL and did not have enough energy to reach the *E* stage of the telescope. The PSD technique was then used to discriminate between heavy fragments and light particles stopping in the same  $\Delta E$  detector. The selection of fission events was achieved by a coincidence method as explained later.

The acquisition system is based on the FAIR readout bus [17]. Data were collected requiring the OR mode between the following triggering conditions: a) coincidences between any PPAC and any BALL particle detector to select the events corresponding to the light particles emitted in the ER channel, b) events detected by any PPAC module to select ER events in single mode, c) twofold events in the F and G ring detectors to select events with at least two fission fragments, and d) coincidences between one detector of the F or G ring and any other particle detector of the BALL to select particles in coincidence with at least one fission fragment. This triggering scheme is very effective for the evaluation of the multiplicities because

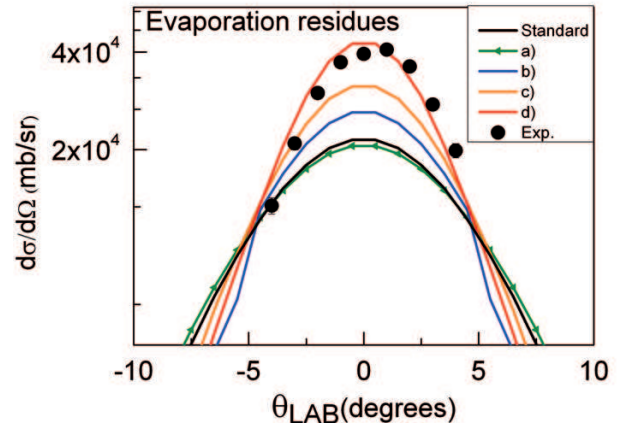


Fig. 2: (Color online) Measured ER angular distribution compared with SM calculations.

it provides, in the same run, for the measurement of the singles and coincidences yields. Consequently, systematic errors are strongly suppressed.

Data sorting and analysis was handled by the software package VISM [18].

## 2.2 ER and FF cross-section measurements

The ER and FF angular distributions were measured in a separate experiment at LNL. The absolute cross-sections were obtained by the numerical integration of the measured angular distributions. We describe here briefly the experimental methods.

### 2.2.1 Evaporation residues cross-section measurement

To detect ERs we used the electrostatic deflector system PISOLO [19]. It allows to measure the differential cross-sections of heavy recoiling products in the angular range  $-10^\circ \div +10^\circ$  with respect to the beam direction. The products coming out of the target pass at first through the electrostatic deflector. The different electric stiffness of the ER and beam-like ions is exploited by applying a strong electric field perpendicular to the beam direction. The beam-like ions are then spatially separated from the heavier products and are stopped in a collimator. The heavier products enter subsequently a TOF-E spectrometer. This is constituted by a micro-channel plate, used as start detector, followed by a large area Si detector used as a stop detector and to measure the energy of the heavy products.

With this system it is possible to separate the ERs from the other reaction products in the forward angles around the beam direction. The main feature of this apparatus is its capability to suppress the beam ions in the TOF-E spectrometer by a factor up to about  $10^8$ . The ER angular distribution is obtained by rotating the whole experimental setup in the horizontal plane. The absolute



Table 1: Proton and alpha particle multiplicities in the ER and pre-scission channels together with the FF and ER cross-sections for 200 MeV  $^{32}\text{S} + ^{100}\text{Mo}$  reaction. The calculation is performed with the parameters which best reproduce the FF channel data. See text for details.

	ER channel		FF channel		$\sigma_{\text{FF}}$ (mb)	$\sigma_{\text{ER}}$ (mb)
	$M_p$	$M_\alpha$	$M_p$	$M_\alpha$		
Exp.	$0.90 \pm 0.14$	$0.56 \pm 0.09$	$0.055 \pm 0.007$	$0.038 \pm 0.005$	$130 \pm 13$	$830 \pm 50$
Calc.	1.44	1.64	0.058	0.034	143	813

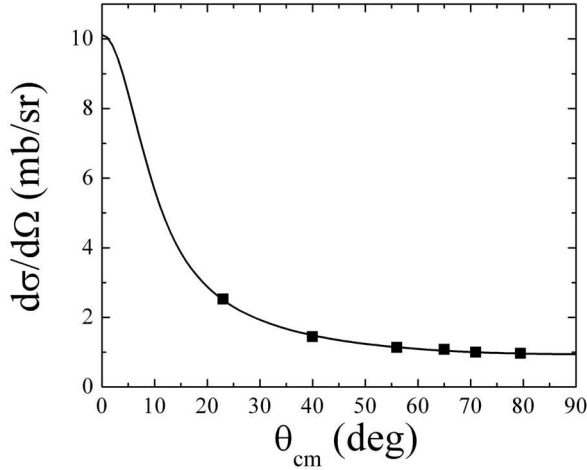


Fig. 3: FF angular distribution.

values of the differential cross-sections were obtained by normalizing the ER yields to the elastic scattering yields obtained by four monitor detectors.

The measured ER angular distribution, shown in fig. 2, was integrated to obtain the ER total cross-section of  $830 \pm 50$  mb. This angular distribution is an additional observable of very valuable use in the analysis discussed later.

### 2.2.2 Fission fragments cross-section measurement

In the same experiment the angular distribution of the FF was measured with a TOF-E spectrometer based on the CORSET setup [20]. The spectrometer consists of an arm that can be mounted inside the scattering chamber at various angles with respect to the beam direction and that allows to measure simultaneously the velocity (via the time of flight) and the energy of a fragment. For the present measurement, the time-of-flight spectrometer consisted of two compact micro-channel plate detectors providing start and stop signals, separated by a flight path of 15 cm. The start detector was placed at 12 cm from the target. To measure the energy, a Si detector was mounted behind the stop detector. The solid angle subtended by the spectrometer was 2.6 msr.

The fragments were detected at six laboratory angles between  $14^\circ$  and  $50^\circ$  and the differential cross-section,

after proper normalization to elastic scattering, was obtained. The angular distribution in the center-of-mass frame is shown in fig. 3 together with the curve which is the fit to the data obtained by using the transition-state model [21]. A cross-section value of  $130 \pm 13$  mb was obtained by integrating the curve.

In table 1 the values of the ER and FF cross-sections are reported. These values determine, in the sharp-cutoff approximation, the angular momentum windows from 0 up to  $67\hbar$  for ER and from  $67\hbar$  to  $72\hbar$  for the FF channels, respectively. These ranges of angular momentum were used in the simulations performed with the SM codes.

### 2.3 LILITA\_N97, PACE2\_N97 and GANES statistical model codes

In this work we have performed a large variety of calculations with the codes LILITA\_N97 [22], PACE2\_N97 [23] and GANES [24] that implement variants of the SM model.

#### 2.3.1 LILITA\_N97

The computer code LILITA [22] models the multistep evaporative decay of a compound nucleus by using the Hauser-Feshbach formulation of the SM in conjunction with the Monte Carlo method. The possible competing decay channels are only neutrons, protons and alpha particles decays. Fission is not considered. The program produces laboratory frame energy spectra and angular distributions for both ER and light particles that either can be obtained in output as histograms or can be constructed from an event-by-event file where the history of each decay step is recorded. This last option is very useful to filter the events with the experimental constraints, for instance, to search for those specific angular correlations measured with the experimental setup.

The code LILITA\_N97 is an extensively modified version of the original LILITA code. New options were included for the transmission coefficients and the level density. Transmission coefficients can now be further chosen between the optical model (OM) [25–27] and the fusion systematics (FS) [28]. Furthermore, modified versions of the Fermi gas level density with different prescriptions of the level density parameter were added along with the following prescriptions for the yrast line: 1) with parameters from the Rotating Liquid Drop Model (RLDM) [29],

2) the Gilbert-Cameron prescription [30], 3) with parameters provided by the user.

### 2.3.2 PACE2\_N97

The code PACE2 [23] simulates the multistep de-excitation of the compound nucleus both through light-particle evaporation and fission decay. Also in this case, light-particle evaporation is implemented according to the Hauser-Feshbach formulation. The fission probability is instead calculated by using the transition-state model and fission barriers are computed with the Finite Range Liquid Drop Model (FRLDM) [29]. The competition between the different decay modes is again treated with a Monte Carlo approach.

The program PACE2\_N97 is a modified version of the code PACE2. It was modified to implement the same options as in LILITA\_N97 and additionally to take into account the fission delay time  $\tau_d$ . In particular, the fission decay width is given by the following formula:

$$\Gamma_f = f(t)\Gamma_{BW}, \quad (1)$$

where  $f(t)$  is a simple step function:  $f(t) = 0$  for  $t < \tau_d$  and  $f(t) = 1$  for  $t > \tau_d$ .  $\Gamma_{BW}$  is the Bohr-Wheeler width [31]. Since the program PACE2\_N97 also includes the fission decay, it was used in our unified analysis of the multiplicities in both the FF and ER channels, and to explore the need for a fission delay time to reproduce our pre-scission multiplicity data.

It is important to remark that the comparison between the predictions of the codes LILITA\_N97 and PACE2\_N97 provided essentially the same results in the ER channel for the system under study, once the same model prescriptions and parameters were chosen. This was an important check for testing the reliability of our SM analysis.

### 2.3.3 GANES

The code GANES [24] was extensively used in the data analysis because it implements a computational model particularly suited to disentangle the contributions to LCP spectra due to several evaporative sources and to calculate angle-integrated multiplicities. LCP spectra in coincidence with FF are characterized by the cumulative contribution of at least three evaporative sources: the composite system prior to scission and the two fission fragments. Each of these sources has specific kinematical and thermodynamical features, and in order to extract the pre-scission multiplicities of the LCP emitted from each specific source a dedicated tool is necessary.

The basic model implemented by GANES is a semi-classical formulation of the SM [24]. The laboratory energy spectra for single-step evaporative emission from excited nuclei are computed with the very efficient weighted Monte Carlo method. This basic physical model is applied to calculate laboratory spectra from the evaporative decay of excited nuclei produced in a variety of reaction classes

like two-body and sequential three-body reactions. We have used GANES to exploit the kinematics of the fission fragments and of the target-like and projectile-like fragments produced in Deep Inelastic Collisions (DIC) as well as to calculate laboratory spectra from the composite nucleus prior to scission and from the fission fragments. The single-step approximation can be considered reasonable in the evaporative emissions from these sources because they are characterized by low multiplicity. The Mass-TKE distributions of the fragments is generated according to the systematics [32]. Furthermore, the code takes into account the geometrical and electronic constraints of the experimental setup.

One important feature of GANES is that the evaporative model takes into account the emitter deformation in a detailed way [33]. The shape of the emitting nucleus is parametrized in terms of the Cassini ovals. The parameter  $0 < \epsilon < 1$  controls the types of axially symmetrical shapes between the two extremes:  $\epsilon = 0$  corresponds to a sphere and  $\epsilon = 1$  corresponds to two touching spheres. The emitter deformation has a strong impact on the energy spectra and the angular distribution with respect to the spin of the emitter. If the excited nucleus has a non-spherical shape the evaporation barrier depends on the birth place of the particle on the nuclear surface, and the moment of inertia is larger. Consequently, emitter deformation affects the mean energy of the charged particles, because of the change in the evaporation barriers, and the out-of-plane angular distribution because of the increase in the moment of inertia [33].

The capability of the code to account for the emitter deformation was exploited in our analysis aimed at unfolding the contributions to the particle spectra in coincidence with FF due to the CN emission prior to scission and to the fragments since the CN is expected to be strongly deformed. In particular, GANES simulations were carried out with two free parameters: the Cassini deformation parameter  $\epsilon$ , and the fraction of emitter excitation energy lost prior to particle emission (FEL) that corresponds to an average fraction of excitation energy lost in the decay prior to charged particle evaporation. This parameter allows to control the high-energy slope of the spectra. The results of this analysis is discussed in sect. 3.2.

## 3 Data analysis procedure and results

### 3.1 Selection of the fission fragments

For the reaction under study, we expect binary fragmentation from fusion-fission and from DIC. The mass distribution of the fission fragments is expected to be symmetric, whereas DIC binary products are characterized by a mass distribution peaked around the projectile and the target masses. The code GANES predicts for the fission folding angle a bell-shaped distribution centered at  $108^\circ$  and ranging from  $104^\circ$  to  $112^\circ$ . For the DIC fragments GANES predicts a folding angle distribution centered at  $104^\circ$  and ranging from  $96^\circ$  to  $112^\circ$ . On the basis of these simulations, fission fragments can be discriminated against DIC

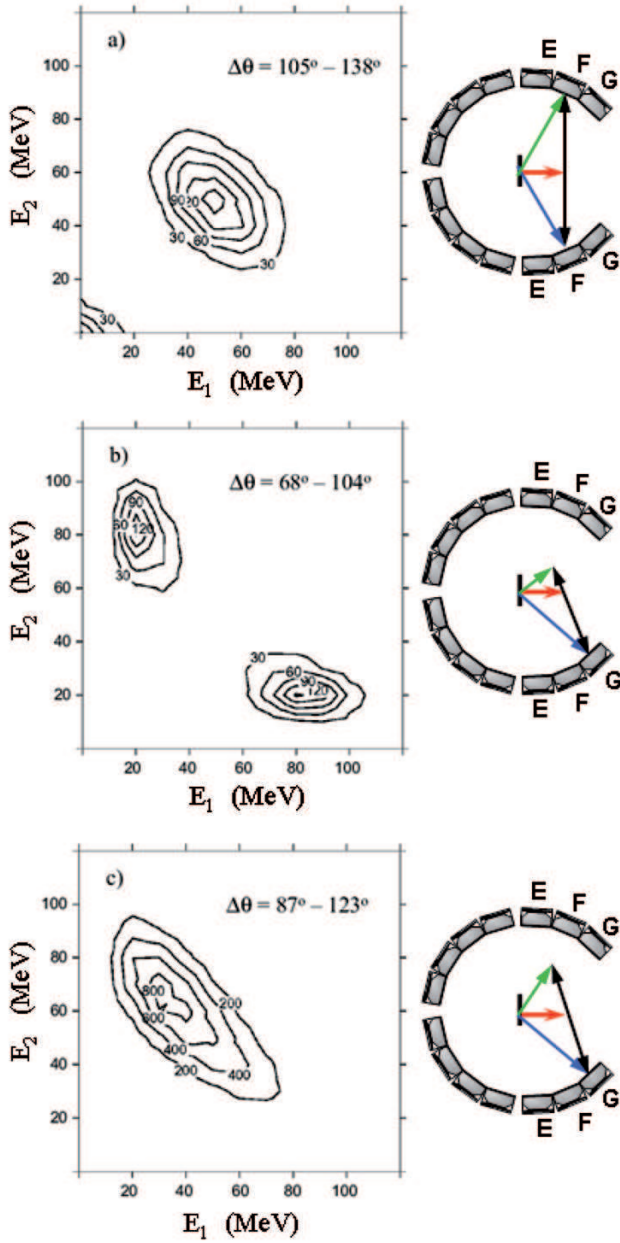


Fig. 4: (Color online) Energy-energy correlation matrix of the fragments measured in coincidence in two opposite detectors of ring F (a), two opposite detectors of ring G (b) and two opposite detectors one in the ring F and one in the ring G (c). The window of the allowed folding angles is also shown for each case.

fragments by energy-energy correlation if the telescopes of the rings F and G are employed to detect two fragments in coincidence. In fig. 4 we show the experimental energy correlation matrices of two fragments detected in coincidence by two telescopes positioned at opposite sides with respect to the beam direction, chosen in the ring F (a), in the ring G (b) and in the ring F and G (c). The experimental windows of the accessible folding angles are as shown in the figure.

Each ring of the BALL consists of 18 telescopes, namely 9 combinations of fragment-fragment trigger detectors, each corresponding to a different azimuthal angle. Each of these 9 combinations defines a different reaction plane. The matrices in fig. 4 were obtained by summing up all the events collected from the 9 reaction planes. The energies  $E_1$  and  $E_2$  are not corrected for pulse height defect.

The plots provide a direct overall view of how the pattern of the energy-energy correlation changes by changing the angle of detection between the two opposite telescopes. This observed pattern is in agreement with GANES predictions. The velocity diagrams on the right side of the figure illustrate the kinematics underlying the symmetric and asymmetric mass splitting. In particular, the velocity vectors are the average values obtained by the simulation. In case (a), the two telescopes are placed symmetrically around the beam direction, and because of the linear momentum and energy conservation, mostly symmetric mass splitting can be detected, considering the folding angle covered by the two opposite detectors and their respective angular openings. Consequently, the two fragments result with about the same kinetic energy and velocity. In case (b), even though the two telescopes are placed symmetrically around the beam direction, the symmetrical splitting is not detected because there is no such kinematic solution for the selected folding angle range. Indeed, the possible solution is only for the asymmetric mass splitting, which means that the lighter (heavier) fragment comes out with the largest (smallest) velocity in the center-of-mass frame. This corresponds to the velocity diagram at the side of fig. 4. The  $E_2$  vs.  $E_1$  correlation reflects this kinematic condition. Case (c) is an intermediate configuration, both asymmetric and symmetric mass splitting are allowed. According to the simulations, case (a) is compatible with symmetric mass splitting, case (b) is compatible with the presence of fragments from DIC. The same simulation confirms that case (c) corresponds to a pair of opposite detectors centered around the most probable folding angle for fission and allows for the detection of the whole fission mass distribution. A possible contamination of DIC fragments in case (c) is predicted to be limited to the regions nearly close to those of the energy-energy matrix of case (b). The extent of such contamination can be estimated from the number of events in both ridges and is found to be negligible in case (c). Consequently, we assume that fragments detected in opposite detectors, one in the ring F and the other in the ring G, are associated with the fission process. Therefore, our analysis was focused on the data corresponding to the F-G correlation.

### 3.2 Particle emission in the fission channel

Laboratory energy spectra of protons and alpha particles measured in triple coincidence with fission fragments in Ring F and Ring G were built by taking advantage of the  $8\pi$ LP array spherical symmetry. The 9 reaction planes offer a valuable mean to sum up properly the particle energy spectra corresponding to the same correlation angle. For



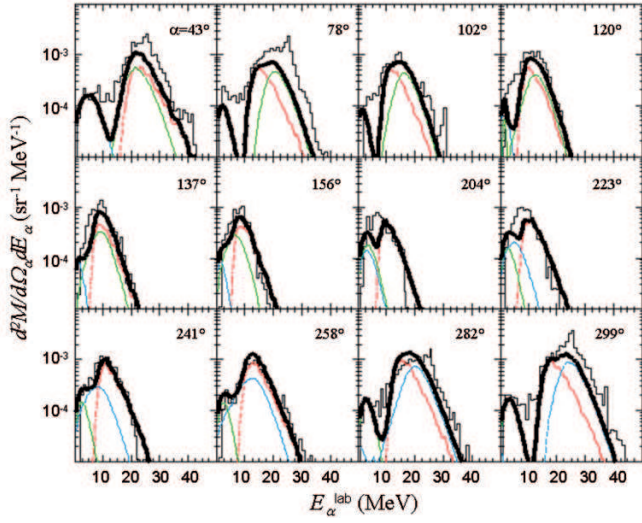


Fig. 5: (Color online) Experimental (histogram) in-plane multiplicity spectra of alpha particles in coincidence with fission fragments detected in the rings F and G. The results of a Monte Carlo simulation are also reported (for details see text).

this purpose, we transformed the polar and azimuthal laboratory angles  $\vartheta$  and  $\phi$  of each detector to an in-plane angle ( $\alpha$ ) and an out-of-plane angle ( $\beta$ ) with respect to each trigger reaction plane. The range of values of  $\alpha$  is  $0^\circ$ – $360^\circ$ , whereas  $\beta$  ranges from  $0^\circ$  to  $90^\circ$ . A position of a detector in the reaction plane is characterized by  $\beta=0$ . The resulting number of spectra is 12 in-plane and 56 out-of-plane. Figure 5 shows, for alpha particles, the experimental differential multiplicity energy spectra (histograms) for the 12 in-plane angular correlations ( $\alpha \neq 0$  and  $\beta=0$ ), and fig. 6 shows the out-of-plane multiplicity spectra ( $\alpha \neq 0$  and  $\beta \neq 0$ ) for a subset of the total available spectra. The multiplicity spectra are obtained by normalizing the area of each spectrum to the number of fission events measured by the trigger detectors.

In order to extract the pre- and post-scission angle-integrated multiplicities, particle spectra were analysed assuming three evaporative sources: the composite nucleus prior to scission (CE) and the two fully accelerated fission fragments (F1 and F2). We have used a well-established procedure that employs the code GANES [24, 33–35] and that takes advantage of the different kinematics of the three emission sources, as will be described in detail. In this procedure, proton and alpha particle evaporative spectra are computed separately for each emitting source in the experimental detection conditions within the window of angular momentum associated to FF. In our case the window is  $67$ – $72\hbar$  as extracted from the channel cross-sections  $\sigma_{\text{ER}}$  and  $\sigma_{\text{FF}}$ . The calculated spectra, for each emitting source, are afterwards normalized to the experimental spectra at the angles where their contribution is kinematically separated from those of the other sources. The normalization at the appropriate angles fixes the intensity of the contribution of each source at all the other angles, as imposed by the angular distributions from

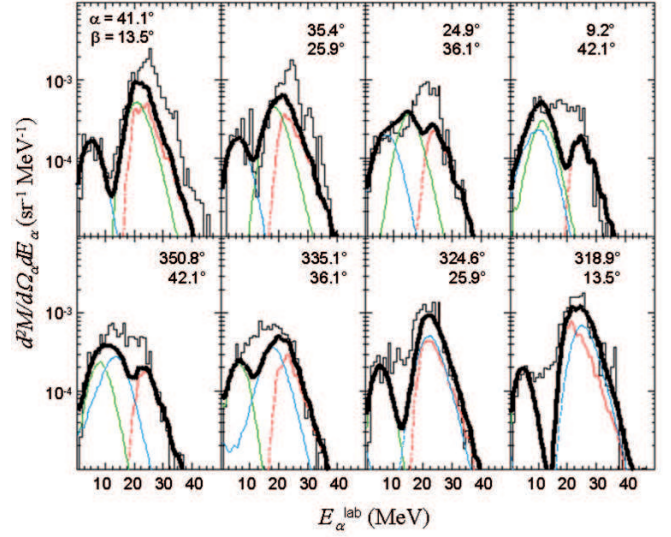


Fig. 6: (Color online) Experimental (histogram) out-of-plane multiplicity spectra of alpha particles in coincidence with fission fragments detected in the rings F and G. The results of a Monte Carlo simulation are also reported (for details see text).

GANES. Finally, the integration by GANES over  $4\pi$  of the resulting angular distributions provides the pre- and post-scission multiplicities.

An iterative procedure was developed and applied to optimize the normalization of the three components to the data. This iterative procedure is summarized as follows. Once the normalization angles for each emitting source is chosen, GANES is run with an initial set of input parameters. Next: i) for each emitting source, a least mean square fit is applied to normalize the calculated spectrum of the chosen angle relative to the single source to the experimental one; ii) at every LCP angle, a sum spectrum of all the components is computed; iii) with the calculated sum spectra and the experimental ones a  $\chi^2$  value is extracted. The steps i) to iii) were then iterated for a grid of values of the deformation parameter  $\epsilon$  and the fractional energy loss FEL for the CE component in order to minimize the  $\chi^2$ . In this procedure, the composite system prior to fission is considered deformed, whereas fission fragments are considered spherical throughout the calculations. Owing to the complexity of the CE emission, these parameters are the most significative ones, while those for F1 and F2 emission usually do not need to be changed as they are reasonably well fixed by the systematics.

A guide for choosing the normalization angles is the velocity vector diagram as shown in fig. 7 for the alpha particles emitted in the reaction plane and simulated by the code GANES. In the figure the arrows with origin in the center of the target indicate the CN velocity and the average velocities of the fission fragments detected in the rings F and G. The radius of each of the three circles, which are centred at the tip of the velocity vectors, represents the average velocity of the alpha particles in the emitter reference frame, namely the composite system (dot-dashed line) and the fission fragments (dashed line for F1 and solid line for F2). The laboratory average particle

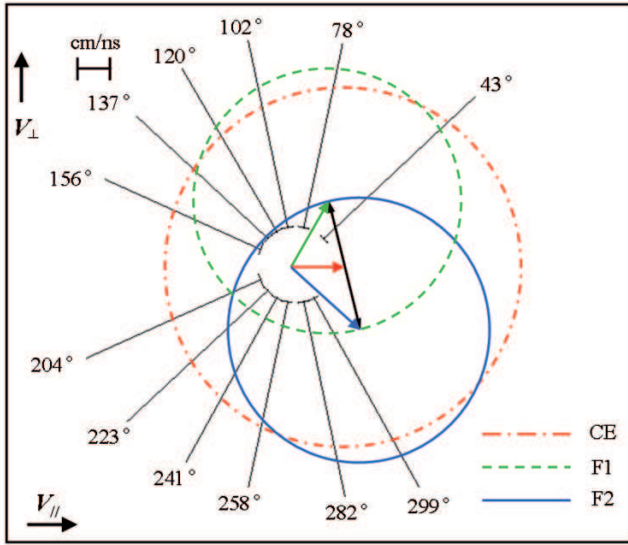


Fig. 7: (Color online) In-plane velocity diagram of alpha particle emission from the composite system prior to scission and from fission fragments.

velocities for a specific emitting source are given by the vectors with origin in the center of the target and ending on the points of the corresponding circumference. The radial lines indicate the laboratory emission angles observed in our experiment and corresponding to the particle spectra in fig. 5, the observed velocity thresholds being also indicated by short bars normal to the lines.

By inspecting the velocity diagram of fig. 7, it is possible to identify the in-plane angles which favor the kinematic separation of one component from the others. For instance, evaporation from the composite system is expected to be relatively well separated from F1 and F2 components at 204° and 223°. From 241° to 299° the F1 component is expected to be well separated from the F2 and CE components, while F2 emission appears to be separated from F1 and CE components in the angular range 43°–156°. This behavior can be recognized in the particle energy spectra of fig. 5. Similar considerations can be worked out for the out-of-plane emission.

The curves superimposed on the histograms in fig. 5 and fig. 6 represent the calculated multiplicity spectra for CE (dot-dashed curves), F1 (dashed line) and F2 (light solid line), along with their sum (dark solid line). In fig. 8 we show the multiplicity spectra and the calculation performed with GANES for the protons in the out-of-plane configuration. In our data the best fit of the energy spectra provides for the CE component  $\epsilon = 0.8$  (axis ratio  $b/a = 3$ ) and  $FEL = 0.15$ . It is important to stress that reproducing both the energy spectra and the angular distributions imposes very strong constraints on the model parameters.

The effect of the deformation can be clearly seen in the center-of-mass angular distribution with respect to the spin as shown in fig. 9 for alpha particles. Spherical (dotted-line) and deformed nuclei (solid line) with  $b/a=3$

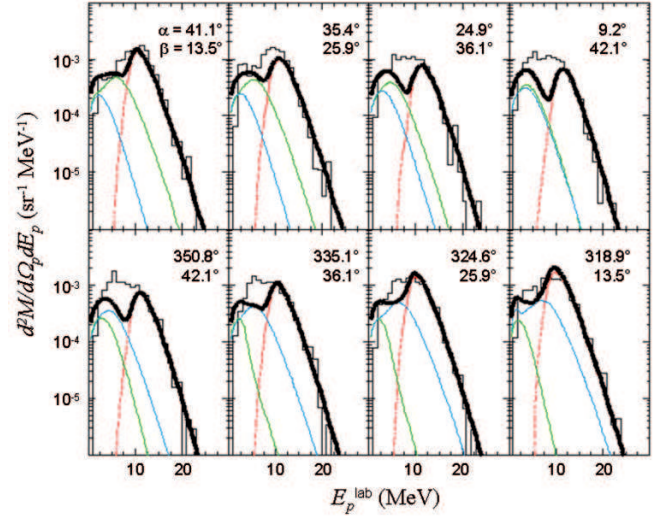


Fig. 8: (Color online) Experimental (histogram) out-of-plane multiplicity spectra of protons in coincidence with fission fragments detected in the rings F and G.

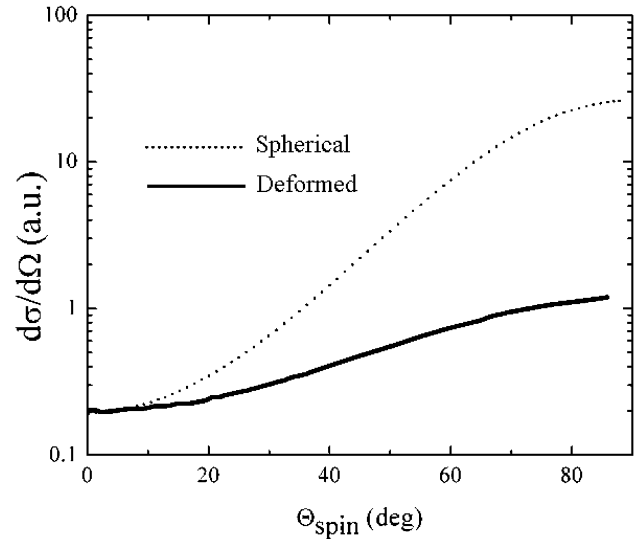


Fig. 9: Alpha particle angular distribution with respect to the spin of the composite system calculated with the code GANES.

and  $J = 70\hbar$  were assumed in the calculation. The effect of the increase in the moment of inertia is to reduce the angular anisotropy. It is important to remark that the change in the anisotropy is also determined, to a lesser extent, by the reduction of the emission barrier. The resulting changes, as function of  $b/a$ , in both quantities are necessary to reproduce our proton and alpha particle energy spectra. Assuming the evaporation from the three emitting sources, the bulk of the experimental spectra is reasonably well reproduced over a wide angular coverage of the detector array, ensuring the reliability of the extraction procedure for the pre- and post-scission multiplicities. Table 1 shows the resulting proton and alpha particle multiplicities.

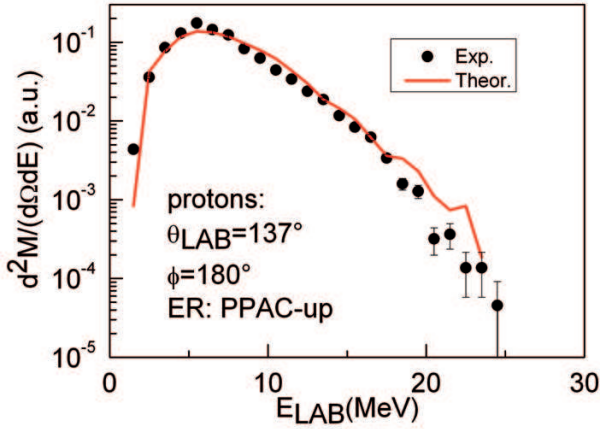


Fig. 10: (Color online) Proton energy spectrum measured in coincidence with ERs, compared to the predictions of the statistical model, using standard parameters.

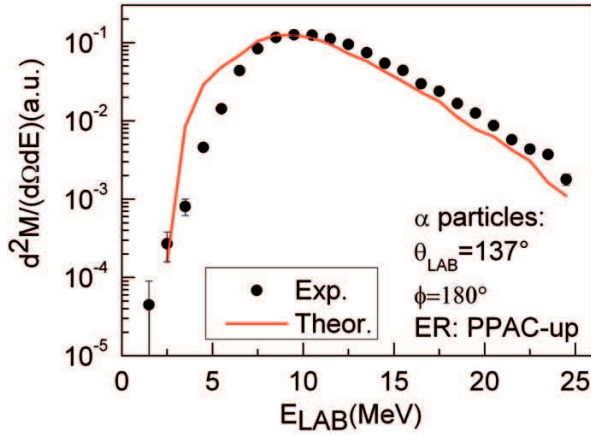


Fig. 11: (Color online) Alpha particle energy spectrum measured in coincidence with ERs, compared to the predictions of the statistical model, using standard parameters.

A closer inspection of the spectra reveals indeed contributions not accounted for by the CE, F1 and F2 components. Two types of contributions are present: a slight excess of high-energy particles at few forward angles, and a surplus of particles with energies between those corresponding to CE and F1 or F2. These two types of contributions have already been observed in other experiments of the same kind as presented here [34] and have been ascribed to pre-equilibrium and near-scission emission [36–38], respectively. These two processes are not relevant in our case and therefore, were not taken into account in our analysis.

### 3.3 Particle emission in the ER channel

Particle spectra in the ER channel were measured as LCP-ER coincidence events by selecting the ER peak in the time spectra produced by the PPAC detectors. As an example, in figs. 10 and 11 the energy spectra obtained at

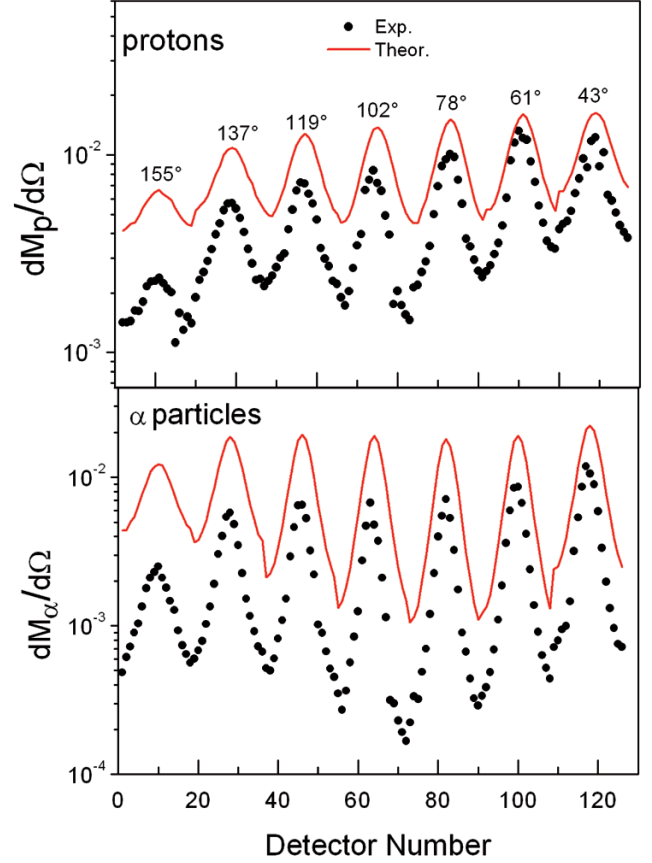


Fig. 12: (Color online) Proton and alpha particle multiplicities measured with the BALL detectors in coincidence with the ERs detected in the PPAC-up, compared to the predictions of the statistical model using standard parameters. Each peak corresponds to the detectors of a ring defined by the polar angle indicated in the figure. Each point of a peak corresponds to a different azimuthal angle from 0 to 360°.

the laboratory angle of 137° are presented for protons and alpha particles, respectively. The PACE2\_N97 simulation is also shown and will be discussed in the following section.

The LCP differential multiplicities were measured by the BALL-PPAC coincidences and by normalizing the total counts of the spectra to the number of the ER single events. In fig. 12 the differential multiplicities for protons and alpha particles in coincidence with the PPAC-up are shown as a function of the BALL detector number starting from the most backward angle. In the figure the polar angle of each ring of the 8πLP BALL is indicated. As mentioned before, for a fixed polar angle, the detectors span in azimuthal angles from 0 to 360° giving rise to peaks in the angular correlation. This behaviour is due to a combined effect of kinematics and angular momentum of the composite system. In particular, the maxima correspond to the events where ERs and LCP are in-plane on the opposite sides of the beam direction, while the minima occur when ERs and LCPs are in-plane on the same side of the beam direction.



By angle-integrating the differential multiplicities of the BALL detectors alone we obtained the partial proton and alpha particle multiplicities corresponding to 80% of  $4\pi$  for the LCP and to the angular position and solid angle of the PPAC for the ER. We call this quantity the experimental *BALL-PPAC* multiplicities. From these quantities, the total LCP multiplicities were extracted by using the statistical model according to the following procedure.

From the simulations, we first obtained the total LCP multiplicities, assuming both the LCPs and the ERs to be emitted over  $4\pi$ . Then, the detailed geometry of our detecting system was included and the *BALL-PPAC* multiplicities were obtained. Ratios of the calculated total to the *BALL-PPAC* multiplicities for protons and alpha particles were thus obtained. These ratios are rather weakly dependent on the statistical model parameters and the two codes LILITA.N97 and PACE2.N97 provide the same results. These ratios are determined by the angular distributions of both LCP and ER in the laboratory frame and by the geometry and solid angles covered by the apparatus. As the angular distributions in the laboratory frame are mainly determined by kinematics, angular momentum effects play a minor role, and only a weak dependence of the SM parameters is expected on these ratios. The final values of these ratios are  $1.3 \pm 0.2$  and  $1.7 \pm 0.3$  for protons and alpha particles, respectively. The quoted uncertainty of 15% results from the range of values obtained by varying the SM parameters. This means that, the SM indicates that with the detectors of the BALL in coincidence with a PPAC in a fixed position we measure only a fraction of the total multiplicity of protons and alpha particles. The total proton and alpha particle multiplicities can therefore be obtained by multiplying the respective partial experimental multiplicities by 1.3 and 1.7. The different ratios found for protons and alpha particles reflect primarily the different kinematics of the two particles, implying a lower degree of focalization for protons compared to alpha particles at forward angles (not covered by our detection system). By applying this procedure we obtained the values reported in table 1.

## 4 Statistical model analysis

First we recall the list of the measured quantities which represent an extended set of observables. Proton and alpha particle multiplicities in the pre-scission and in the ER channels, particle energy spectra in both channels, and particle-ER angular correlations were extracted. In addition, FF and ER angular distributions and cross-sections were measured. Proton and alpha particle multiplicities in the ER and pre-scission channels together with the FF and ER cross-sections are presented in table 1.

The data were analysed in the framework of the statistical model as implemented in the PACE2.N97 code. The main goal was to extract the fission delay of the fissioning system, constraining the model on a wide set of data. We started our calculations adopting parameters, appropriate for the mass and excitation energy of the system under study. If we limit our analysis to the pre-scission LCP

multiplicities and FF cross-section, as usually done [1] in fission dynamic studies, the fission data can be reasonably well reproduced without any delay as shown in table 1. In the calculation we used  $a_\nu = A/9$ ,  $a_f/a_\nu = 1.04$  where  $a_\nu$  and  $a_f$  are the level density parameters for particle evaporation and fission, respectively, RLDM yrast line and OM transmission coefficients. From this result, one could conclude that no dynamical effects take place in this decay, in contrast with the systematics [13], although a different combination of input parameters does not exclude the presence of a relatively small fission delay. On the other hand, with the same parameters, the model strongly overestimates the ER particle multiplicities. As regards the LCP energy spectra in this channel, we obtain a reasonable agreement for proton spectra while a deviation is observed mainly at the low-energy side of the alpha particle spectra (figs. 10 and 11). Furthermore, the model is not able to reproduce the angular correlations (fig. 14) for both particles and the angular distribution of the ERs (fig. 2). This is an evident contradiction: if the model is not able to reproduce the data in the ER channel, except for the ER cross-section, the same model cannot be taken as a reliable tool to estimate the fission time scale through the pre-scission LCP multiplicities.

In order to investigate to what extent the model is not able to reproduce the whole set of experimental data with a unique set of SM input parameters we performed an extensive analysis with the code PACE2.N97 adopting different prescriptions and with parameters ranging in a wide interval of values, also including values not usually adopted for the mass region and the excitation energy of the system under study. Calculations were carried out adopting three different prescriptions for the yrast line: i) Gilbert Cameron [30], ii) rotating liquid drop model (RLDM) and iii) the rigid sphere (RS) assuming  $r_0 = 1.2$  fm for the calculation of the moment of inertia. Different prescriptions were also used for the level density parameter  $a_\nu$  for particle evaporation: i) a constant value ranging from  $A/6$  to  $A/12$ , ii) inclusion of shell effects [39] with a damping term [40] as a function of the excitation energy and iii) a temperature-dependent prescription [41]. Transmission coefficients derived from the optical model (OM) [25–27] and from the fusion systematics (FS) [28] were used. In the case of FS transmission coefficients, the values of the barrier curvatures were constrained requiring the best reproduction of the low-energy part of particle spectra. Calculations were constrained by the fusion cross-section  $\sigma_{\text{fus}} = 958 \pm 52$  mb obtained by the sum of the measured ER and FF cross-sections. To modulate evaporation-fission competition, different values of fission delay and  $a_f/a_\nu$  ratio were adopted.

In fig. 13 we show the measured multiplicities for protons and alpha particles in the ER and FF channels, and the measured channel cross-sections, compared to the calculated values, as a function of the ratio  $a_f/a_\nu$ . In the figure the results correspond to the four different prescriptions labeled as a), b), c), d) of table 2. These prescriptions were chosen among many combinations of the leading parameters that allow to explore the full range of variability



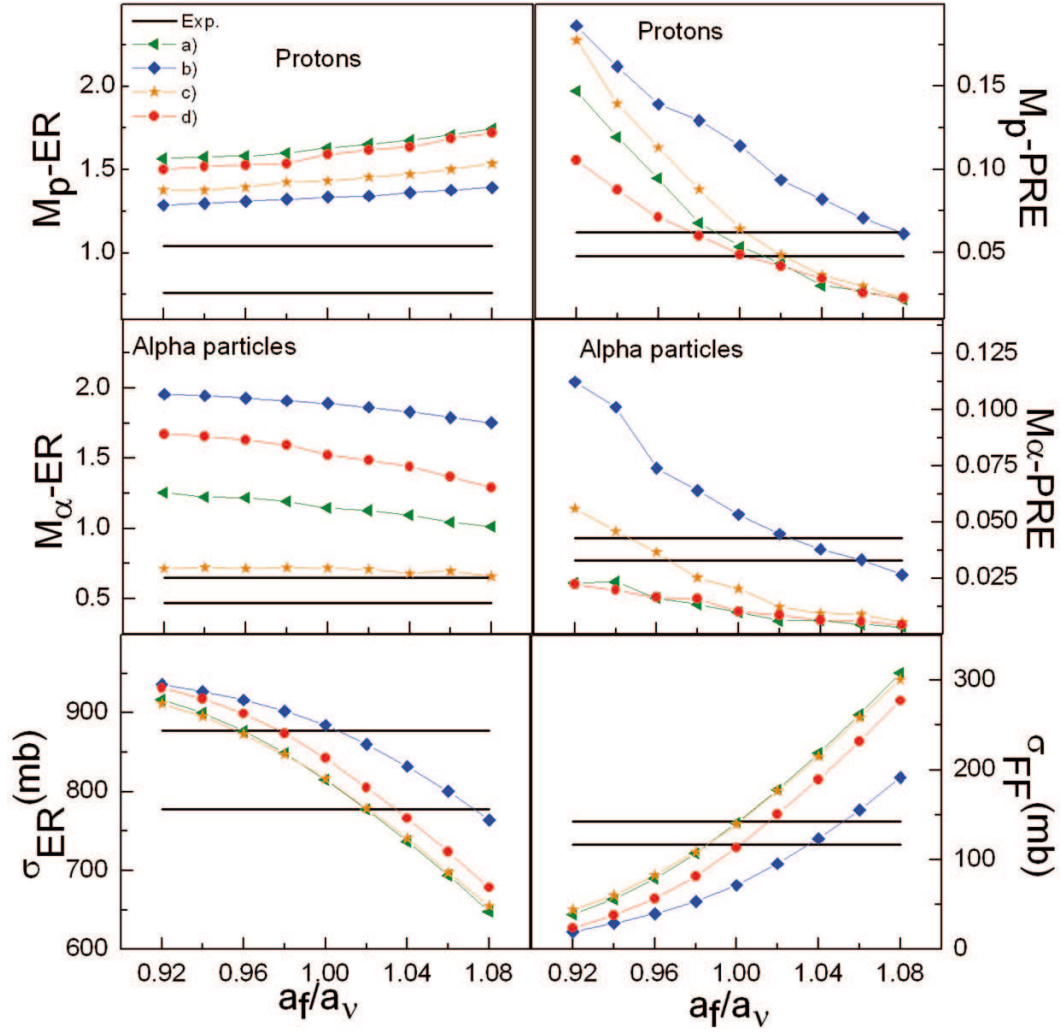


Fig. 13: (Color online) Measured evaporative (ER)(left side) and pre-scission (PRE)(right side) LCP multiplicities together with the FF and ER cross-sections (horizontal full lines indicating lower and upper limits of the multiplicity values due to the experimental errors), compared to the prescriptions of the statistical model changing: i) the level density parameter ( $a_\nu$ ), ii) the yrast line, iii) and the transmission coefficients. For details see text.

Table 2: Sets of inputs adopted in the calculations with the statistical model for 200 MeV  $^{32}\text{S} + ^{100}\text{Mo}$  reaction.

SM inputs	$a_\nu$	Yrast line	Transmission coefficients
a)	$A/6$	RS	OM
b)	$A/12$	RLDM	OM
c)	$A/6$	RS	FS
d)	$A/6$	RLDM	OM

of the calculated values of the observables under examination. No fission delay was included in the calculations. The shell and temperature effects on the  $a_\nu$  parameter, as well as the Gilbert Cameron prescription for the yrast line produce only minor changes in the results and therefore, are not presented here. By looking at fig. 13, one can observe that pre-scission multiplicities and ER and fission

cross-sections show a significative dependence on the SM prescriptions as well as on the ratio  $a_f/a_\nu$ . Although a set of input parameters reproduces these observables, as shown in table 1, ER-LCP multiplicities are not reproduced irrespective of the input parameters. The model is not able to reproduce the observables altogether. Here we will discuss how the results for the ER channel depend on a single SM input of table 2, while keeping the others unchanged. Higher values of  $a_\nu$  lower the alpha particle multiplicities, while those for protons are enhanced, (see the prescriptions b) and d) in fig. 13). Compared to the OM transmission coefficients, those derived from FS provide lower values for both proton and alpha particle multiplicities (see prescriptions a) and c)). The dependence of the calculated multiplicities on  $a_f/a_\nu$  appears to be relatively weak. Finally, we observe, as expected, a strong sensitivity of the alpha particle multiplicity on the yrast line: assuming the RS yrast line (prescription a)), we obtain a strong

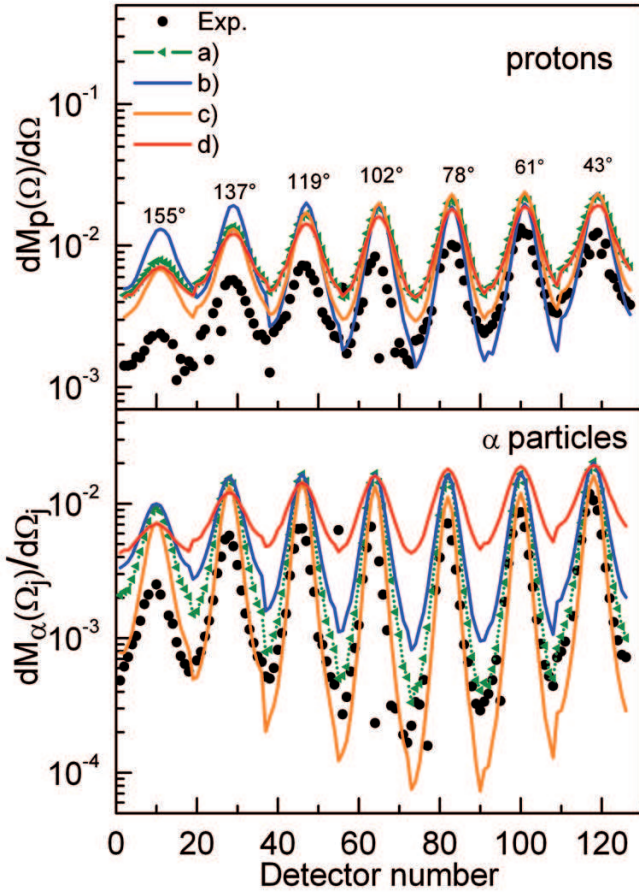


Fig. 14: (Color online) Proton and alpha particle multiplicities measured with the BALL detectors in coincidence with ERs detected with the PPAC-up, compared to the predictions of the statistical model.

reduction of this quantity, with respect to that obtained with RLDM yrast line (prescription d)).

The ER-LCP angular correlations appear to be a good probe as they are very sensitive to the SM parameters. In fig. 14 we show the experimental proton and alpha particle differential multiplicities as a function of the detector position compared to the SM calculations performed using the a), b), c) and d) prescriptions. The differences among the different prescriptions are more evident in the alpha-ER correlation with respect to the proton-ER one. All calculations are carried out for the value  $a_f/a_\nu = 1$ . As a general behavior, for a fixed yrast line, increasing  $a_\nu$  produces a very strong reduction in the maximum-to-minimum (MTM) ratios of the angular correlation (see the prescriptions b) and d)). Going from the yrast line calculated using the RLDM to the yrast line assuming the nucleus as a rigid sphere with  $r_0 = 1.2$  fm, that means a decrease of the moment of inertia, we observe an increase in the MTM ratio for proton and alpha particle angular correlation. This behavior, in the case of alpha particles, indicates that  $a_\nu = A/6$  provides results more close to the experimental data. The sensitivity to the transmission coefficients is not very strong and the

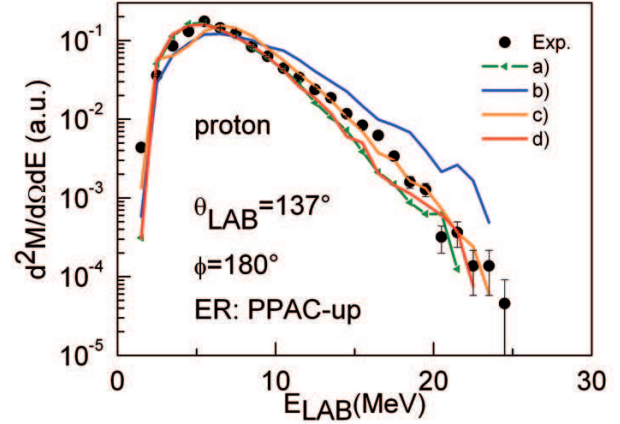


Fig. 15: (Color online) Proton energy spectrum measured in coincidence with ERs, compared to the predictions of the statistical model. For details see text.

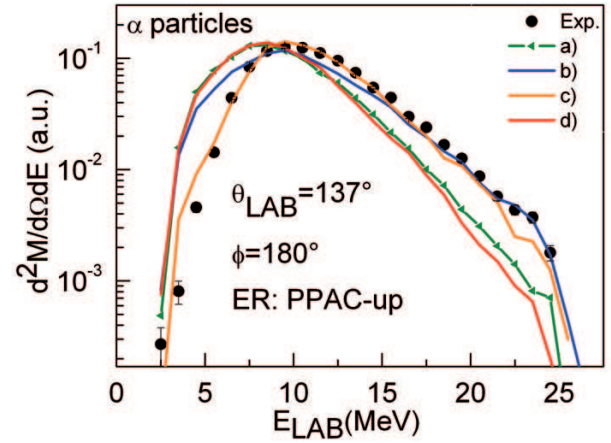


Fig. 16: (Color online) Alpha particle energy spectrum measured in coincidence with ERs, compared to the predictions of the statistical model. For details see text.

amplitude is larger in the case of FS with respect to the OM coefficients (see the prescriptions c) and a)).

The experimental ER angular distribution is compared with the predictions of the SM in fig. 2. Significant deviations are observed for options a), b) and c) while option d) provides results relatively close to the experimental data.

The comparison of the measured ER-LCP energy spectra with the predictions of the SM are shown in figs. 15 and 16 for protons and alpha particles, respectively. For the protons options a) and d) underestimate the high-energy side while option b) overestimates it. This results from the different level density parameters which provide higher temperatures for options a) and d) with respect to option b). For all these three options, OM transmission coefficients provide a reasonable reproduction of the low-energy part of the spectrum. For option c), the interplay between the level density parameter,  $a_\nu = A/6$  and the FS transmission coefficients results in a good reproduction of the high and very low-energy sides of the spectrum, but the maximum is not reproduced.

Table 3: Comparison of experimental and calculated multiplicities for the ER emission of protons and alpha particles from the compound nuclei with  $A \approx 150$  and  $E_x \approx 100\text{--}200$  MeV.

Reaction	Ref.	$E_{\text{lab}}$ (MeV)	$E_x$ (MeV)	$L_{\text{fus}}$	Experimental		Our calculation	
					$M_p$	$M_\alpha$	$M_p$	$M_\alpha$
$^{32}\text{S} + ^{109}\text{Ag} \rightarrow ^{141}\text{Eu}$	[7]	180	90	75	$1.30 \pm 0.30$	$0.60 \pm 0.10$	1.90	0.80
$^{121}\text{Sb} + ^{27}\text{Al} \rightarrow ^{148}\text{Gd}$	[35]	905	135	84	$1.16 \pm 0.26$	$0.73 \pm 0.17$	1.70	0.95
$^{40}\text{Ar} + ^{\text{nat}}\text{Ag} \rightarrow ^{147,9}\text{Tb}$	[34]	247	128	94	$1.02 \pm 0.20$	$0.50 \pm 0.10$	2.05	0.98
$^{40}\text{Ar} + ^{\text{nat}}\text{Ag} \rightarrow ^{147,9}\text{Tb}$	[34]	337	194	103	$2.10 \pm 0.60$	$1.40 \pm 0.40$	3.10	1.46
$^{60}\text{Ni} + ^{100}\text{Mo} \rightarrow ^{160}\text{Yb}$	[43]	550	251	78	$1.10 \pm 0.15$	$0.58 \pm 0.15$	3.34	3.18
$^{32}\text{S} + ^{100}\text{Mo} \rightarrow ^{132}\text{Ce}$	Present work	200	122	72	$0.90 \pm 0.14$	$0.56 \pm 0.09$	1.44	1.64

As far as alpha particles are concerned, options a) and d) underestimate the high-energy side of the spectrum and overestimate the low-energy one, resulting in an energy shift of the whole calculated spectrum to lower energy. This is due to a combined effect of the level density parameter  $a_\nu = A/6$  and the OM transmission coefficients. For option b), the higher temperature produced by the value  $a_\nu = A/12$  reproduces the high-energy part of the spectrum, while the OM transmission coefficients give an overestimation of the spectrum at low energy. Finally, concerning option c), the combined effects of both the level density parameter  $a_\nu = A/6$  and the FS transmission coefficients result in a good agreement with the data.

Calculations of energy spectra taking into account the nuclear deformation do not support any evidence for deformed emitting nuclei. In particular, we have performed a calculation assuming the radius parameter  $r_0 = 1.45$  fm for the moment of inertia and transmission coefficients with the reduced barriers from systematics [28]. The inclusion of deformation results in a substantial lowering of the average energy of the spectra for both particles, implying a disagreement for all the options in the calculations. At the same time, it produces an enhancement of the multiplicities for both particles, resulting in a larger disagreement with the data. A similar behaviour is observed for the angular correlations, where nuclear deformation produces a reduction of the maximum to minimum ratios.

## 5 Discussion and conclusions

Our SM analysis on the system  $^{32}\text{S} + ^{100}\text{Mo}$  brings out the failure of the model in reproducing the whole set of the data measured for this system. The most striking result is that while the SM, with standard parameters, reproduces the LCP pre-scission multiplicities, which usually would require a fission delay to be introduced in the model, the same model strongly overestimate the LCP multiplicities in the ER channel, irrespective of the SM parameters. In spite of this, both ER and FF cross-sections are reproduced for value of  $a_f/a_\nu \approx 1$ . In other words, even though the ER cross-section, as a bulk observable, is not affected by the detail of the SM, the competition between the different LCP decay modes is not described correctly by any of the used prescriptions. The incorrect description of the LCP decay would affect also the pre-scission channel, mak-

ing the extraction of the fission delay time unreliable. In particular, if the failure of the SM would have a common origin for both the pre-scission and the ER channels, it would bring to an overestimation of multiplicities in both channels. Therefore, the found behaviour makes more difficult to withdraw conclusions about this anomaly of the model considering that LCP multiplicities in the ER channel are expected to be reproduced by the SM. It must be here pointed out that we find the same discrepancy with the codes LILITA\_N97 and GEMINI [42].

The overestimation of the LCP multiplicities in the ER channel was also observed in other systems in the region  $A \approx 150$  and  $E_x \approx 100\text{--}200$  MeV. In table 3 we compare the experimental data taken from the literature with the predictions obtained with the code PACE2\_N97. The shown results are obtained using the most appropriate SM parameters for the mass and energy regions of these systems. One observes that again the SM calculations overestimate the proton and alpha particle multiplicities in the ER channel, excluding the alpha particle multiplicity for the  $^{147,9}\text{Tb}$  at  $E_x = 194$  MeV, which is essentially reproduced. The causes for such an unexpected behavior of the SM can be searched along two lines: either the competition between the different decay channels is not properly accounted for, or we are missing some decay channels, or both. Indications toward the first hypothesis would come from the neutron multiplicity in the ER channel that, unfortunately, is rarely measured. In the case of  $^{60}\text{Ni} + ^{100}\text{Mo}$ , studied in ref. [43], where neutron multiplicity is also measured, our SM calculations, in agreement with those of ref. [44], enhance proton and alpha multiplicities and suppress neutron emission. This might be the case for the other reactions reported in table 3. A rough indication of how much the SM branching ratios should be changed in favor of the neutron emission might be taken from the experimental multiplicities [45]. However, since the branching ratios are strongly dependent on the decay step, empirical constant factors to reduce the strengths do not represent a reasonable approach to this problem, and would open the question on how to use these new parameters in the FF channel. The measurement of the neutron multiplicities in the ER channel is at this point a mandatory task [7].

There is also the possibility of other decay channels not presently considered in the SM code PACE2\_N97, like Intermediate Mass Fragments (IMF). Given the low probability of such emission we do not expect the IMF channel



to be important for the reactions taken under consideration here except for the  $^{60}\text{Ni}+^{100}\text{Mo}$  case, where the excitation energy is high enough to allow for IMF emission. We remark that this is also the only case where the SM gives the largest deviation for both protons and alpha particles. In any case we did not observe any IMF in our data from the system  $^{32}\text{S}+^{100}\text{Mo}$  at  $E_{\text{lab}} = 200$  MeV in coincidence with ER.

In conclusion, the present study indicates some limitations of the statistical model and raises serious doubts on its use for studying the fission process, where dynamical degrees of freedom should be properly accounted for.

One of us (PNN) is grateful to the Istituto Nazionale di Fisica Nucleare (INFN) for financing his stay in Naples, and also wishes to thank the Naples section of INFN for the warm hospitality during his visit. DVS would like to thank the Legnaro section of INFN for their support during his stay in Italy.

## References

1. P. Paul, M. Thoennessen, *Annu. Rev. Nucl. Part. Sci.* **44**, 65 (1994); doi: 10.1146/annurev.ns.44.120194.000433, and references therein.
2. J.P. Lestone, *Phys. Rev. C* **59**, 1549 (1999); doi: 10.1103/PhysRevC.59.1540.
3. A. Chatterjee *et al.*, *Phys. Rev. C* **52**, 3167 (1995); doi: 10.1103/PhysRevC.52.3167.
4. D.J. Hofman, B.B. Back, P. Paul, *Nucl. Phys. A* **599**, 23c (1996); doi: 10.1016/0375-9474(96)00044-9.
5. L. Fiore *et al.*, *Nucl. Phys. A* **620**, 71 (1997); doi: 10.1016/S0375-9474(97)00154-1.
6. V.A. Rubchenya *et al.*, *Phys. Rev. C* **58**, 1587 (1998); doi: 10.1103/PhysRevC.58.1587.
7. E. Vardaci *et al.*, in *Proceedings of the International Symposium on Dynamics Aspects of Nuclear Fission, Casta-Papiernicka, Slovak Republic, October 1998*, edited by Yu.Ts. Oganessian, J. Kliman and S. Gmuca (World Scientific, Singapore, 2000) p. 261.
8. I. Diószegi *et al.*, *Phys. Rev. C* **61**, 024613 (2000); doi: 10.1103/PhysRevC.61.024613.
9. I. Diószegi *et al.*, *Phys. Rev. C* **63**, 014611 (2000); doi: 10.1103/PhysRevC.63.014611.
10. N.P. Shaw *et al.*, *Phys. Rev. C* **61**, 044612 (2000); doi: 10.1103/PhysRevC.61.044612.
11. A. Saxena *et al.*, *Phys. Rev. C* **65**, 064601 (2002); doi: 10.1103/PhysRevC.65.064601.
12. G. La Rana *et al.*, *Eur. Phys. J. A* **16**, 199 (2003); doi: 10.1140/epja/i2002-10091-y.
13. M. Thoennessen, G.F. Bertsch, *Phys. Rev. Lett.* **71**, 4303 (1993); doi: 10.1103/PhysRevLett.71.4303.
14. E. Vardaci *et al.*, *Eur. Phys. J. A* **43**, 127 (2010); doi: 10.1140/epja/i2009-10912-5.
15. E. Fioretto *et al.*, *IEEE Trans. Nucl. Sci.* **44**, 1017 (1997).
16. J.F. Ziegler, J.P. Biersack, U. Littmark, *Stopping and Range of Ions in Solids* (Pergamon Press, New York, 1985).
17. A. Ordine, A. Boiano, E. Vardaci, A. Zaghi, A. Brondi, *IEEE Trans. Nucl. Sci.* **45**, 873 (1998).
18. E. Vardaci, VISM: a Computer Program for Nuclear Data Analysis, Annual Report Carnegie Mellon University, Pittsburgh, USA, 1989.
19. S. Beghini *et al.*, *Nucl. Instrum. Methods Phys. Res. A* **239**, 585 (1985); doi: 10.1016/0168-9002(85)90040-3.
20. E.M. Kozulin *et al.*, *Instrum. Exp. Tech.* **51**, 44 (2008).
21. J.R. Huizenga, A.N. Behkami, L.G. Moretto, *Phys. Rev.* **177**, 1826 (1969); doi: 10.1103/PhysRev.177.1826.
22. Lilita program was written by J. Gomez del Campo and R.G. Stockstad, Oak Ridge National Laboratory Report No. TM7295, 1981 (unpublished).
23. A. Gavron, *Phys. Rev. C* **21**, 230 (1980); doi: 10.1103/PhysRevC.21.230.
24. N.N. Ajitanand, R. Lacey, G.F. Peaslee, E. Duek, J.M. Alexander, *Nucl. Instrum. Methods Phys. Res. A* **243**, 111 (1986) and references therein.
25. J.R. Huizenga, G. Igo, *Nucl. Phys.* **29**, 462 (1961).
26. F.G. Perey, *Phys. Rev.* **131**, 745 (1963); doi: 10.1103/PhysRev.131.745.
27. D. Willmore, P.E. Hudson, *Nucl. Phys.* **55**, 673 (1964).
28. L.C. Vaz *et al.*, *Z. Phys. A* **318**, 231 (1984).
29. A.J. Sierk, *Phys. Rev. C* **33**, 2039 (1986); doi: 10.1103/PhysRevC.33.2039.
30. A. Gilbert, A.G.W. Cameron, *Can. J. Phys.* **43**, 1446 (1965).
31. N. Bohr, J.A. Wheeler, *Phys. Rev.* **56**, 426 (1939).
32. V.E. Viola *et al.*, *Phys. Rev. C* **31**, 1550 (1985); doi: 10.1103/PhysRevC.31.1550.
33. N.N. Ajitanand *et al.*, *Phys. Rev. C* **34**, 877 (1986); doi: 10.1103/PhysRevC.34.877.
34. R. Lacey *et al.*, *Phys. Rev. C* **37**, 2540 (1988); doi: 10.1103/PhysRevC.37.2540.
35. W.E. Parker *et al.*, *Nucl. Phys. A* **568**, 633 (1994); doi: 10.1016/0375-9474(94)90398-0.
36. E. Duek *et al.*, *Phys. Lett. B* **131**, 297 (1983).
37. L. Schad *et al.*, *Z. Phys. A* **318**, 179 (1984).
38. E. Vardaci *et al.*, *Phys. Lett. B* **480**, 239 (2000); doi: 10.1016/S0370-2693(00)00407-X.
39. S.K. Kataria, V.S. Ramamurthy, S.S. Kapoor, *Phys. Rev. C* **18**, 549 (1978); doi: 10.1103/PhysRevC.18.549.
40. A.V. Ignatyuk *et al.*, *Sov. J. Nucl. Phys.* **21**, 612 (1975).
41. J.P. Lestone, *Phys. Rev. C* **52**, 1118 (1995); doi: 10.1103/PhysRevC.52.1118.
42. R.J. Charity, Computer code GEMINI (unpublished).
43. M. Gonin *et al.*, *Phys. Lett. B* **217**, 406 (1989); doi: 10.1016/0370-2693(89)90069-5.
44. J.M. Alexander *et al.*, *Proceedings of the Symposium on Nuclear Dynamical and Nuclear Disassembly, 1988, Dallas, Texas, USA*, edited by J.B. Natowitz (World Scientific, Singapore, 1989) p. 211.
45. J.L. Wile *et al.*, *Phys. Rev. C* **51**, 1693 (1995); doi: 10.1103/PhysRevC.51.1693.